doi:10.20944/preprints202206.0295.v1

*Type of the Paper (Article)*

# Microstructural study of CrNiCoFeMn high entropy alloy obtained by selective laser melting

**Enrico Gianfranco Campari [1]*, Angelo Casagrande [2]**

[1] Department of Physics and Astronomy, Alma Mater Studiorum-University of Bologna, Viale Berti Pichat 6/2, 40127 Bologna, Italy
[2] Department of Industrial Engineering, Alma Mater Studiorum-University of Bologna, Viale Risorgimento 4, 40136 Bologna, Italy; angelo.casagrande@unibo.it
* Correspondence: enrico.campari@unibo.it; Tel.: +39 051 2095148

**Abstract:** The high entropy alloy (HEA) of equiatomic composition CrNiFeCoMn and with FCC crystal structure was additively manufactured with a selective laser melting (SLM) process starting from mechanically alloyed powders. The as produced alloy shows fine nitride and σ phase precipitates, which are Cr-rich and stable up to about 900 K. The precipitates increase in number and dimensions after long-period annealing at 900-1300 K, with a change in the HEA mechanical properties. Higher aging temperatures in furnace, above 1300 K, turn the alloy in a single FCC structure, with disappearance of the nitrate and σ phase precipitates inside the grains and at the grain boundaries, but with still a presence of a finer Cr-rich nitride precipitation phase. These results suggest that the as-produced HEA is a supersatured solid solution at low and intermediate temperature with nitrides and σ nanostructures.

**Keywords:** high entropy alloys, selective laser melting, microstructure, mechanical properties, strengthening mechanism.

## 1. Introduction

The concept of High Entropy Alloy (HEA) was proposed and published in 2004 [1-3] and the unique properties of these alloys have attracted attention from research groups all over the world. The pioneering studies by Cantor et al. were the first to report that an equiatomic alloy consisting of the five transition metals Cr, Mn, Fe, Co and Ni crystallized as a single solid solution [1,4] in the as cast and in the homogenized state.

The first HEAs generation could contain five or more main elements with the concentration of each element in the range 5-35 at. % [3]. The alloys present a high mixing entropy in their liquid state [4] and thus can form simple solid solution structures (e.g. FCC, BCC and HCP) in place of intermetallic phases. Some promising technological characteristics of HEAs are high hardness [5], good wear resistance [6], excellent strength at both high and low temperatures [7-9] and generally a good resistance to oxidation and corrosion [10]. The unique properties of the HEAs are ascribed to the inherent properties of multicomponent solid solution formation, such as distorted lattice structures [11], cocktail effect [12], sluggish diffusion [5] and formation of nanoscale deformation twins [8]. From a metallurgical standpoint, the suppression of the brittle intermetallic phases in such alloys is to be regarded as a really interesting feature. As recalled by other authors, the CrNiMnCoFe HEAs are considered stable disordered supersaturated FCC solid solutions with high ductility and remarkable fracture toughness [9]. HEAs usually exhibit good thermal stability [7,8,13], which is commonly attributed to sluggish long-range substitutional diffusion because of the lack of a major diffusion element and the need for cooperative diffusion of constituent atoms in order to have proper composition partitioning. Consequently, diffusion-related processes, including crystallization and grain growth, are expected to be slow in HEAs.

The belief that the equiatomic CoCrFeNiMn alloy be an example of high entropy alloy with a single disordered solid solution structure was recently challenged by the discovery of second phases in the alloy after low-temperature annealing. Despite the use of specific processing conditions (prolonged annealing or severe plastic deformation prior to annealing) these studies, contrasting with the previous literature, show that a second phase formation can occur in this alloy because the sluggish diffusion in HEAs is not a guarantee of a stable structure and precipitates would be nucleated in case of prolonged annealing times [14-16]. Increased configurational entropy in same cases may stabilize single-phase solid solution microstructures [2, 4]. Generally, however, this effect is insufficient to override the driving forces that favor the formation of secondary phases by precipitation or decomposition. Thus, high configurational entropy can not be considered a useful a priori predictor of whether a high-entropy alloy will form thermodynamically stable single-phase solid solutions or not [17].

For a CrCoMnFeNi alloy to be used in industrial applications, it is critical to investigate both the behavior of this HEAs during the prolonged use at high temperature and the manufacturing processing, not to mention an accurate investigation on the microstructural evolution. In fact, precipitates could lead to relevant changes in the alloy mechanical properties, either increasing the strength or embrittling the alloy. In both cases it is important to control the new phase precipitation or dissolution upon heat treatment. Moreover, the kinetic and the mechanisms of a second phase precipitation into an FCC HEAs are still poorly understood and this spur to further investigate them. Furthermore, it is proved that secondary phases may contribute significantly to the HEAs properties, and it was reported that HEAs can overcome the strength-ductility trade-off when containing two or more phases [17, 18].

With the aim to obtain a better understanding of the various factors that affect phase stability and therefore mechanical properties in high-entropy alloys, we undertook the present investigation on CoCrFeMnNi to determine what happens when the starting, mechanically pre-alloyed powders, are melted by SLM (selective laser melting) in additive manufacturing [19, 20].

This processing method has the advantage of overcoming several limitations of traditional processing methods. For instance, the ability to net-shape manufacture specimens with a high geometrical complexity without the use of dies. SLM was chosen because of its flexible layer-by-layer increase control feature. SLM does not require a vacuum environment and its equipment is therefore simpler than that of selective electron beam melting under vacuum (SEBM). It provides cooling rates up to $10^5$ K/s, while those of conventional melting processes (casting or welding) are typically less than 100 K/s. Therefore, SLM yields finer grains, a fine cellular dendrite structure and substructures within the grain, which improves the overall mechanical performance of the final components [21]. In fact, hardness and tensile properties, at low and high temperature, are superior compared to alloys obtained with traditional casting and recrystallization [22-24].

Effect of the non-equilibrium processing of SLM is also a great amount of residual stresses, a dense dislocations network, impurities and fine precipitation phases at boundaries [25]. This defective state is considered in this work as responsible for both mechanical properties and microstructure evolution during high temperature aging. Specifically, we report about the tetragonal $\sigma$ phase formation in FCC CoCrFeMnNi after a thermomechanical processing comprising a room temperature thickness reduction of 95% and subsequent prolonged annealing. Prolonged annealing times were used because of the sluggish diffusion effect that slows down phase transformation. In addition, cold working was used to accelerate phase precipitation [26, 27].

Although it is possible to use them as structural materials in high temperature environments, studies on equiatomic CoCrFeMnNi HEA produced by additive manufacturing have been limited to manufacturing, microstructural analysis and room temperature tensile properties [28-32]. There have been no studies that investigated the effect of the unique microstructure of SLM-built HEA on high-temperature mechanical properties and deformation mechanism. Owing due to that, objective of this work is to document the fine secondary sigma phase precipitation in as built state induced by SLM technology. Being present from the beginning, a prolonged annealing is not required in order to see it appear, as is the case for HEAs produced with the traditional melting process [13, 15, 16]. In particular, this phase, together with a further nitride precipitation due to the nitrogen protective atmosphere, is the unavoidable consequence of the thermal cycles that accompany the layer by layer growth of the alloy. Whereas up to a certain working temperature fine precipitates can play a reinforcing role, starting from a temperature of about 950 K, the sigma phase tends to swell and to preferentially place itself on the grain boundaries of the alloy. This in turn can lead to a significant reduction of the mechanical and chemical properties. This is described in the following and confirmed by a mechanical characterization with microhardness and hardness measurements that correlates with the microstructural evolutions that occur during aging.

## 2. Materials and Methods

For this study, a nominally equiatomic High Entropy Alloy is produced by a selective laser melting process. Co, Cr, Fe, Mn and Ni powders, with purity greater than 97 % at. were supplied by Sigma Aldrich (Darmstadt, Germany). The powders are mechanically alloyed in an inert Argon atmosphere, using a Retsch (Haan, Germany) PM 100 high energy planetary ball mill and steel balls. Treatment cycles lasting 15 minutes each with a 5 minutes break between them for a total grinding time of 45 hours are used [33]. Break time is used to avoid overheating.

The selective laser melting apparatus, used to produce samples with volume 50x5x5 $mm^3$, is a SISMA MYSINT100 RM (Vicenza, Italy). A high purity Nitrogen atmosphere is used in order to minimize oxidation during the production process. Melting does not take place until Oxygen level drops below the set limit threshold, which is 0.5%. The machine process parameters are H = 0.05 mm, F = 200 $J/mm^3$, recoater rate= 70/150 mm/s with a constant deposition thickness and spot diameter of 20 μm and 50 μm, respectively. The samples surface perpendicular to the growth direction is divided into 6 slices filled according to a chessboard strategy [34].

Sample in the: (1) as built state, (2) cold rolled state, (3) after annealing at 1170 K for 100 h and (4) after thermomechanical treatments into the temperature range 723-1423 K in 100 K steps for 25 h, are sectioned to the deposition direction and are prepared by standard grinding and polishing methods. This includes polishing with diamond suspension down to 1 μm and finishing with colloidal silica solution with a particle size of 0.05 μm.

In all cases, subsequent phase characterization to identify the crystalline structures is carried out by X-ray diffraction (XRD) and by SEM-FEG-EDS-EBSD. XRD analyses are performed with an X'Pert PRO Panalytical diffractometer (Malvern, UK) equipped with a proportional gas detector in a $\theta$-$2\theta$ configuration in the angular range from 10° to 120° using Cu K$\alpha$ radiation ($\lambda$=0.15406 nm). In order to speed up the formation and precipitation of intermetallic phases, a thermomechanical process comprising an 95% thickness reduction by cold plastic deformation at room temperature of the as cast alloy and subsequent prolonged annealing for 25 h, in the temperature range 723-1423 K with 100 K steps, is performed. Microstructural investigations are carried out on cross sections of all samples by an optical microscope and by a field emission scanning electron microscope (SEM-FEG) Tescan MIRA3 (Brno, Czech Republic) equipped with an EDS (energy dispersive spectroscopy) microanalyzer Bruker (Billerica, Massachusetts, US) Quantax. The calculate semi-quantitative EDS analyses, for each phase, are averaged out of five values.

In addition, crystallographic orientation and grain size is analyzed by electron backscattered diffraction (EBSD). EBSD maps are made with Quantax EBSD detector on as built, cold deformed, annealed and re-crystallized samples to document the FCC matrix alloy and the precipitation secondary phase. The EBSD data are recorded and analyzed using the Bruker Esprit software. Prior to any optical or electron observation, samples are polished and chemically etched with a thermal treatment at 473 K in a gliceregia solution composed of 1 $HNO_3$ + 3 HCl + 3 Glycerol. As regards mechanical properties, micro hardness Vickers is evaluated in this study through indentation tests carried out with a VOLPERT tester (Zell am Main, Germany).

## 3. Results and Discussion

### *3.1. Mechanically alloyed HEA*

Morphology and particle size distribution of the mechanically alloyed powders are reported in figure 1. The dimensional range distribution is obtained by means of a laser meter Mastersizer 2000 ver. 5.2 of Malvern Instruments (Malvern, UK). The corresponding X-ray diffraction, figure 2a, mainly shows the reflections of a single FCC phase, together with a weak presence of a secondary phase and Iron oxides.

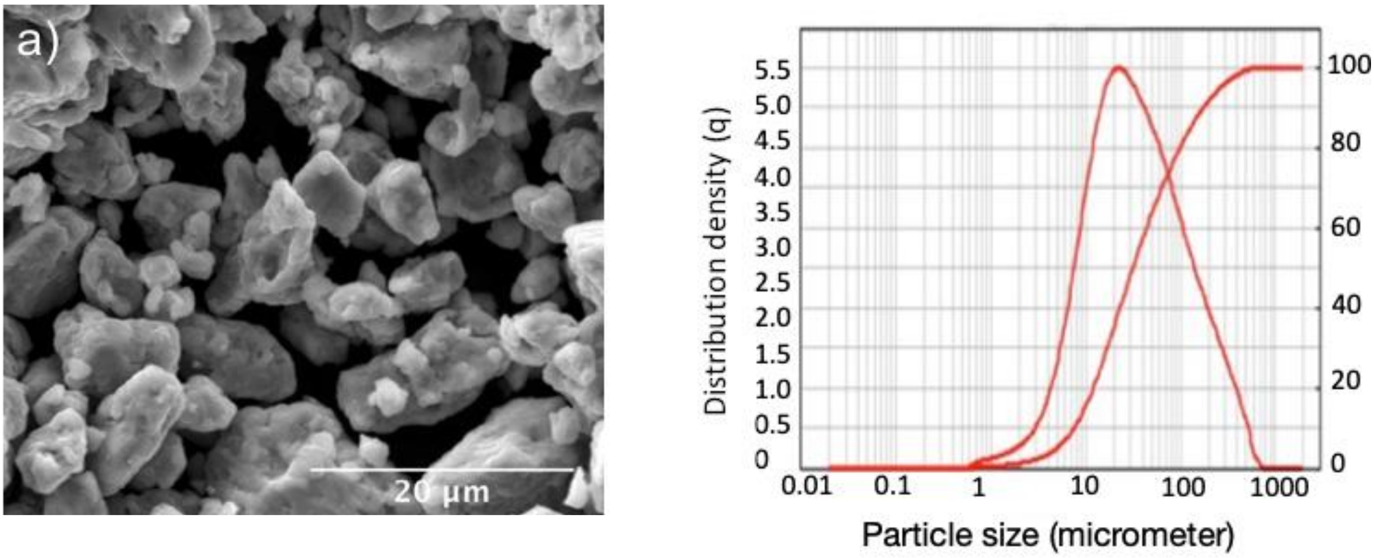

(a) (b)

**Figure 1.** a) Morphology of the mechanically alloyed powders; b) particle size normalized and cumulative distribution.

Oxides are probably due to surface oxidation, for the high surface reactivity of these powders, particularly in the case of Iron. Mechanical alloying does not bring about spherical dust formation, as obtained with the (much more expensive) gas atomization technology. As shown in figure 1b, most powders fall within a range between 10 and 100 µm. By the use of a sieve it will be possible in the future to optimize the particle size distribution up to an appropriate average particle size. A dimensional optimization of the powders will lead to a more uniform microstructure, with dimensionally homogeneous melt pools and increased mechanical properties because of macro porosity reduction.

Figure 2b documents the FCC crystallographic homogeneity throughout the entire thickness of each sample obtained by SLM. XRD is repeatedly performed after thinning a sample by abrasion. Number 1 refers to XRD before abrasion and number 6 to the innermost section after 5 abrasions whose overall removed thickness is 0.5 mm.

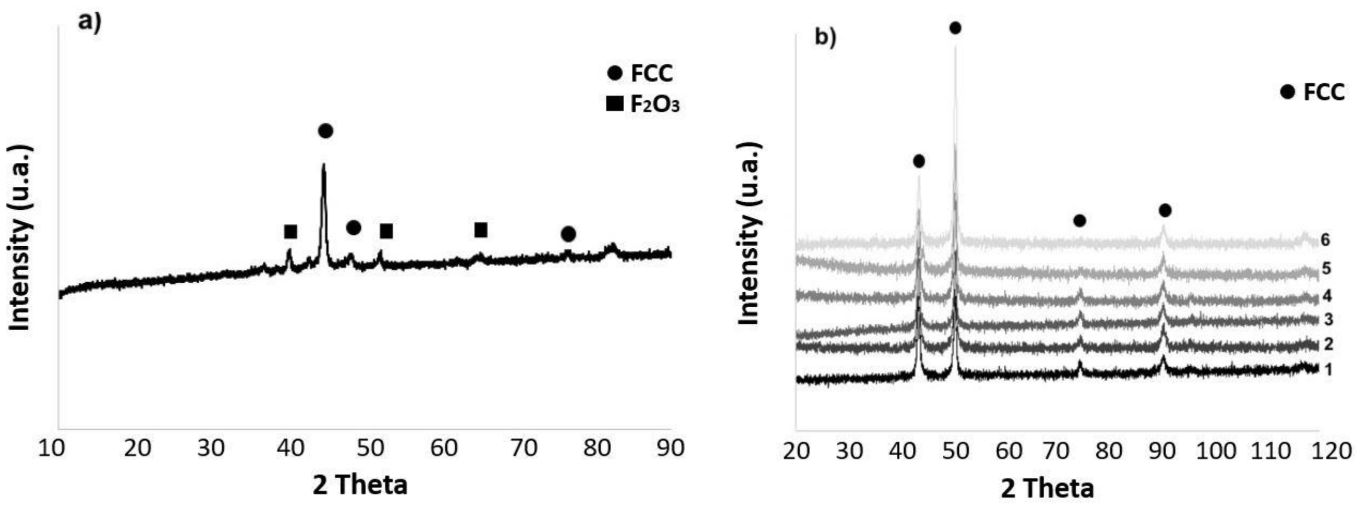

(a) (b)

**Figure 2.** a) XRD of mechanically alloyed powders; b) XRD of the HEA after layer by layer abrasion (from 1 to 6). Overall removed thickness is 0.5 mm.

### *3.2. Microstructure of selective laser-melted equiatomic CoCrFeMnNi high-entropy alloy as built.*

The optical microstructures obtained on transversal sections of the as built SLM samples are shown in figure 3. The image shows the typical melt pools generated by the laser beam, whose depth is also depending on the powder grain size non-uniformity. It is also possible to observe a layered morphology of thickness between 100 µm and 200 µm, depending on the thickness of the deposited powder bed.

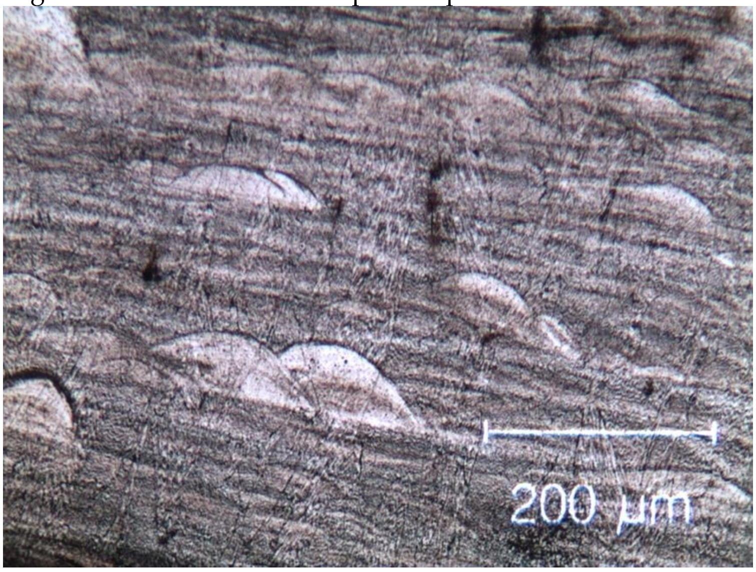

**Figure 3.** Optical micrographs of the as built SLM HEA observed in transversal section with melt pots due to the laser beam.

Due to the locally intense power delivered to these powders, strong junctions are formed between the layers. As visible in figure 4, the most common morphology observed in this alloy when produced by SLM are columnar grains aligned towards the build direction [35]. Columnar grain growth and grain orientation are induced by the rapid cooling conditions and from re-melting due to successive layers deposition. Inside the grains very fine dendritic structures, which grow in the direction of the thermal gradient, are also produced. These are clear evidences that the morphology, size, direction and texture of samples are influenced by the process parameters. These in turn affect the mechanical properties of a component directly assembled in near net shape.

Figure 5a shows a SEM image on a plane perpendicular to the build direction and figure 5b the corresponding EBDS map. Very small precipitation of an intermetallic phase identified as sigma phase is visible (blue), in an FCC matrix, whereas XRD analysis on the same plane (figure 2b), only identifies an FCC structure. Based on the findings from EBSD, XRD and EDS analysis, reported in table 1, the produced alloy is confirmed to basically have an FCC structure and a good equiatomic compositional homogeneity.

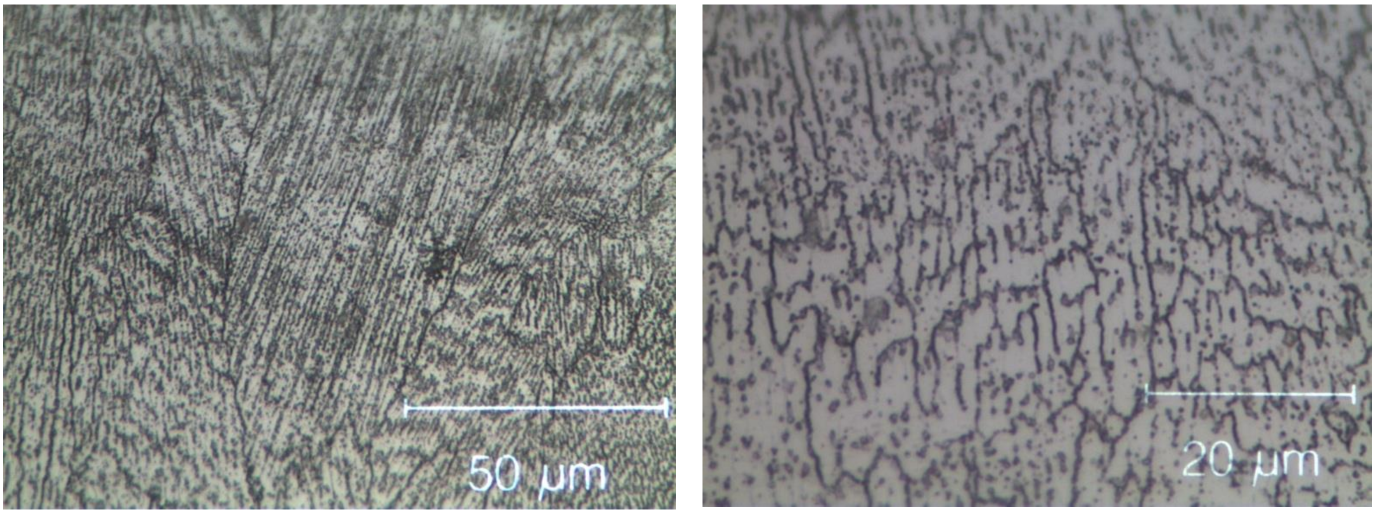

(a) (b)

**Figure 4.** Optical micrographs of the as built SLM HEA observed in transversal section. (a) Columnar grains aligned towards the build direction. (b) Dendritic structures inside the grains.

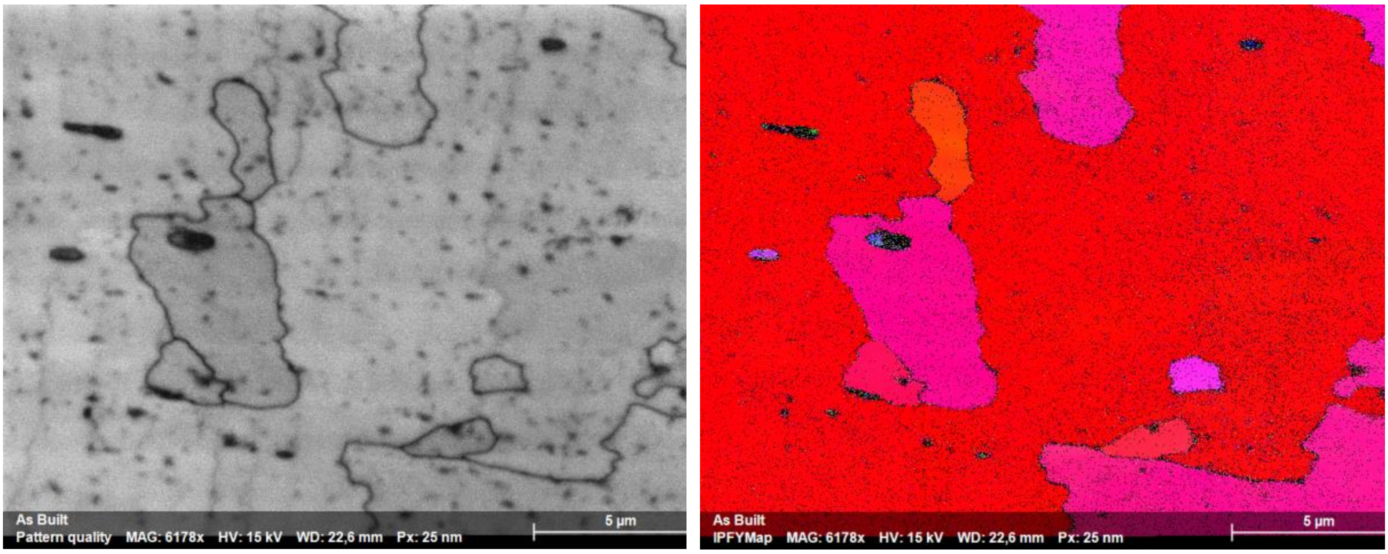

(a) (b)

**Figure 5** (a) Cross-sectional image of the as built alloy, (b) corresponding EBDS map, with FCC matrix in red-pink color and sigma phase precipitates in blue color.

**Table 1.** Semiquantitative EDS chemical analysis (atomic %) of as built alloy.

| Element: | Nitrogen | Chromium | Manganese | Iron | Cobalt | Nickel |
|---|---|---|---|---|---|---|
| Atomic composition (%): | 1.2 | 20.3 | 19 | 20.1 | 19.4 | 20 |

As already mentioned, there is a surface oxides contribution associated with the powder high reactivity. In fact, visible in the microstructures of as built samples, figure 5, and samples aged up to 823 K, figure 6 and figure 7, the solid FCC solution exhibits a fine dispersion of randomly distributed oxides. Such oxides were previously observed in arc-melted CrCoMnFeNi by other Authors [37]. Even finer precipitates cannot be seen below this annealing temperature, see figure 8, since both σ phase and the other precipitates mostly nucleate and grow at temperatures between 900 K and 1300 K [37]. Based on a critical review of the literature, it is worth emphasizing that it is still not established whether and which kind of precipitates are present in the as-built CoCrFeMnNi alloy produced by SLM [38].

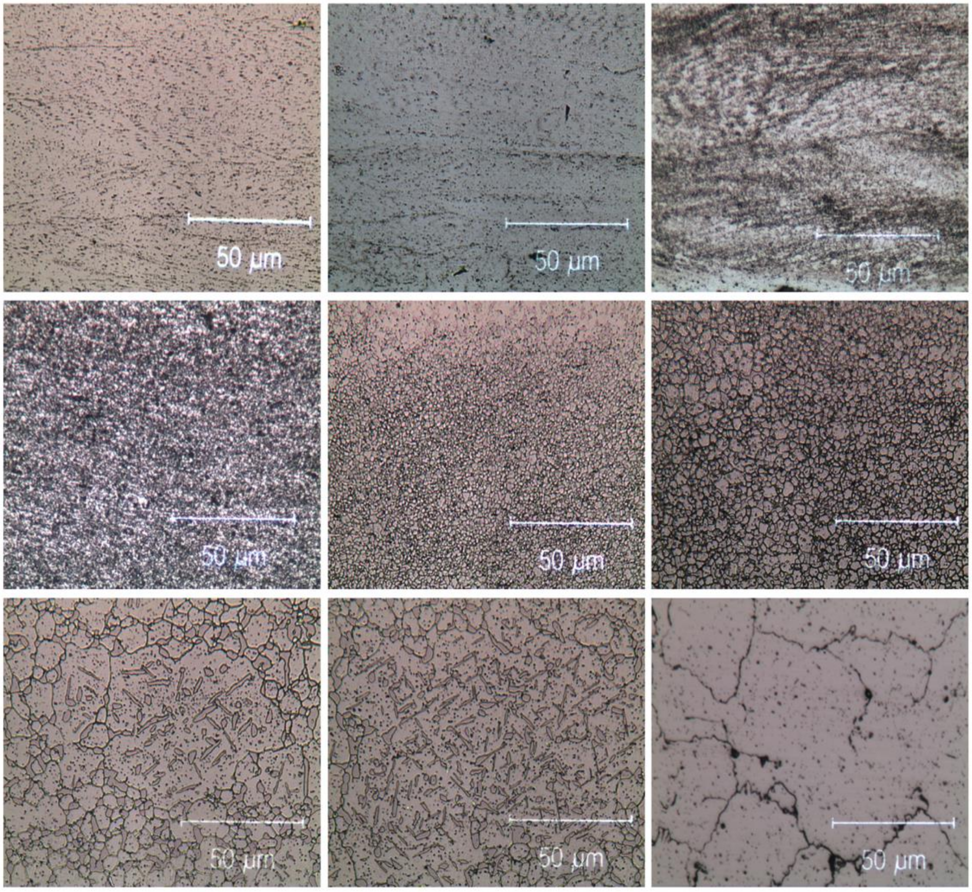

**Figure 6.** Optical transversal sections of cold rolled and annealed samples. Annealing temperatures is, from left to right and top to bottom: 723 K, 823 K, 923 K, 1023 K, 1103 K, 1223 K, 1323 K, 1423 K.

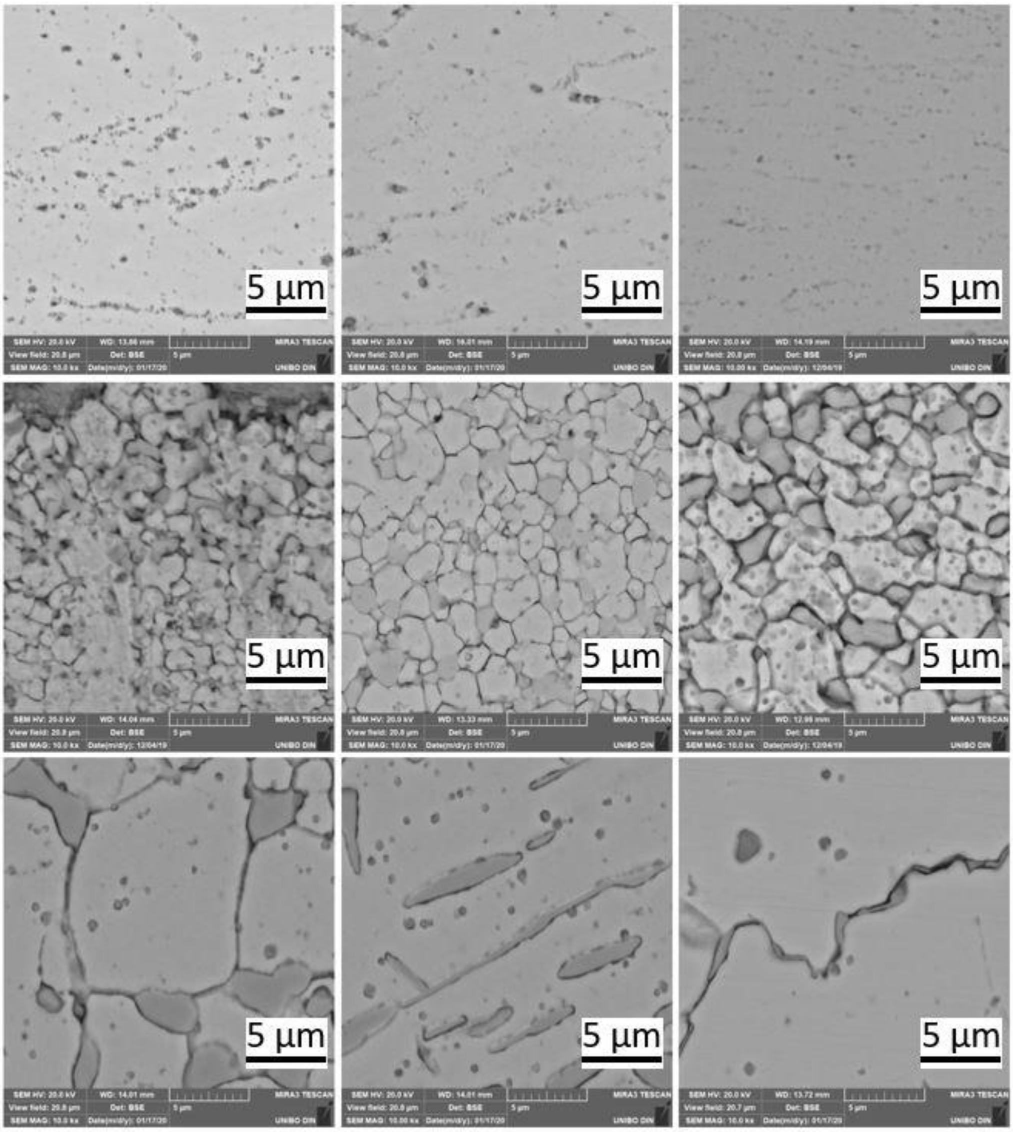

**Figure 7.** SEM-FEG transversal section microstructures of cold rolled and annealed samples. Annealing temperatures is, from left to right and top to bottom: 723 K, 823 K, 923 K, 1023 K, 1103 K, 1223 K, 1323 K, 1423 K.

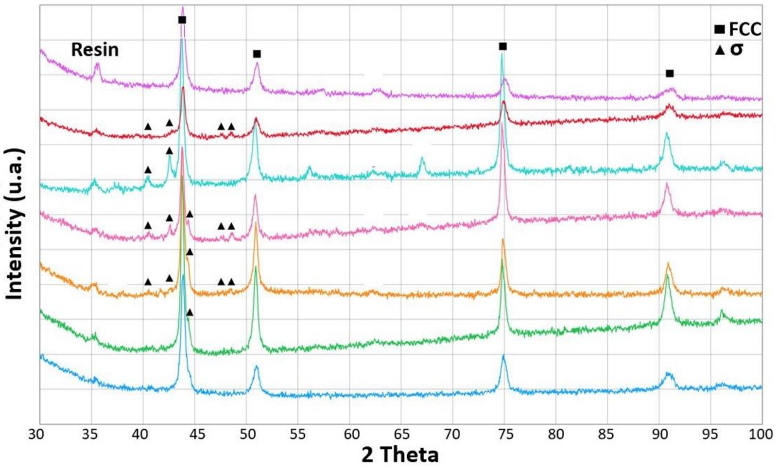

**Figure 8.** XRDs of cold rolled and annealed samples at temperatures between 723 K and 1423 K. Temperature is increasing in 100 K step bottom up. The sequence is: 823 K (blue), 923 K (green), 1023 K (orange), 1123 K (pink), 1223 K (light blue), 1323 K (red), 1423 K (magenta).

Fine precipitates formation at the edge of microdendritic structures are documented in the BSE high resolution images of figure 9 and the EDS microprobe analysis of figure 10. Black precipitates are observed. They are nitrides, around which other precipitates with nanometric size grow. They are due to σ phase. This arrangement, with σ phase growing around nitrides, suggest that at first nitrides appear and then the σ phase is formed by heterogeneous nucleation. σ phase and other precipitates mostly nucleate and grow at temperatures between 850 K and 1250 K, as also observed by other authors [38]. This peculiar microstructure occurs because Nitrogen interstitial diffusion during the SLM process, in the melted state, is fast and the subsequent rapid cooling does not allow the achievement of a stationary condition.

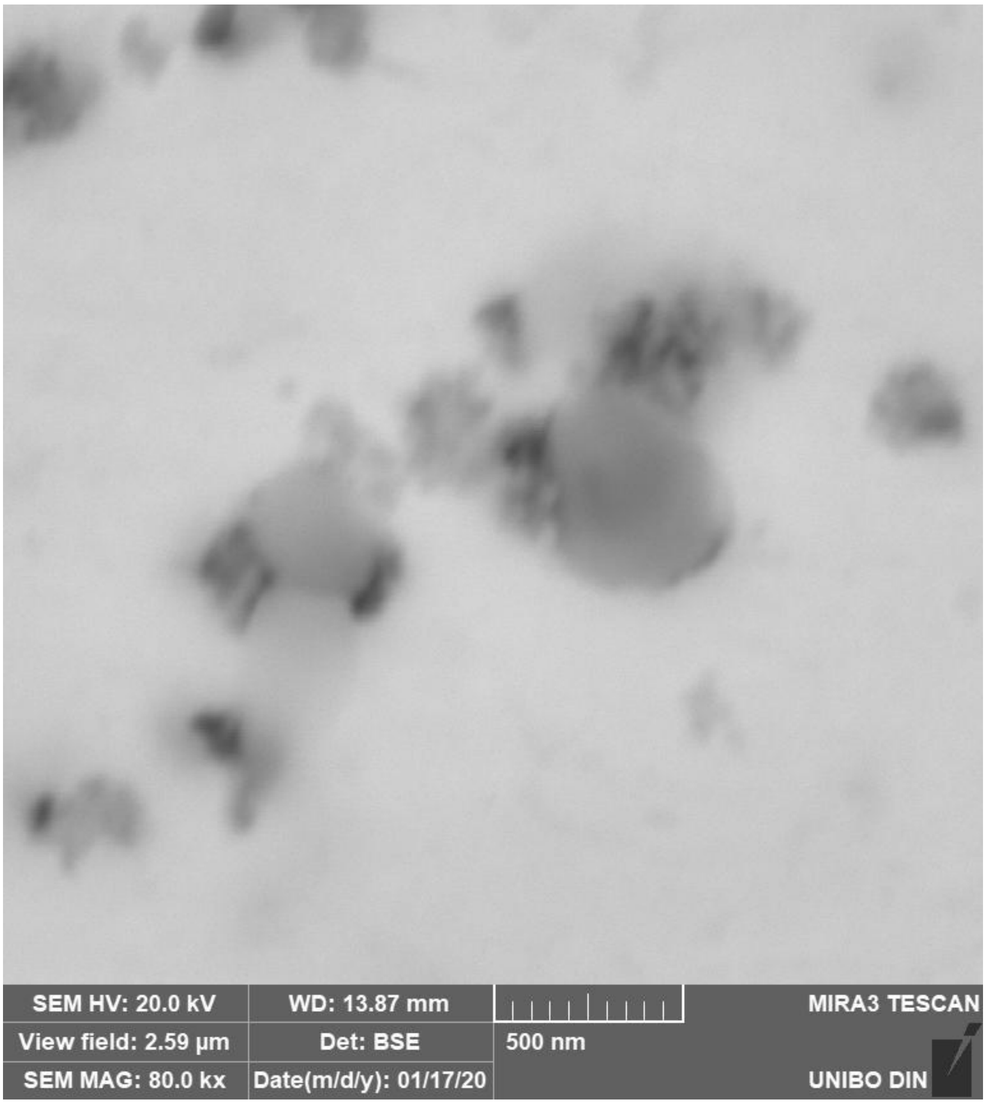

**Figure 9.** SEM FEG high resolution precipitates image in an as built sample.

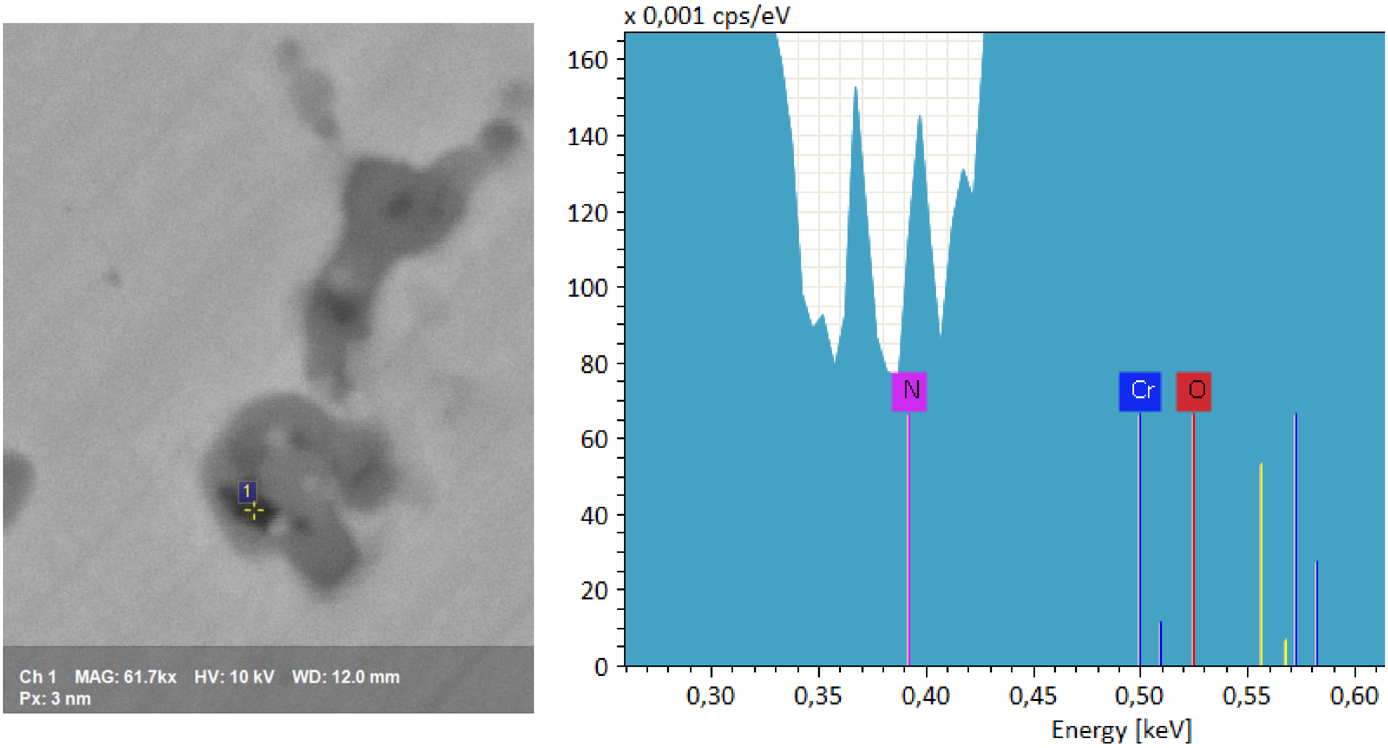

(a)

(b)

**Figure 10.** (a) SEM FEG high resolution precipitates image in an as built sample. (b) EBDS spectrum of the black area of (a) containing a nitride fine precipitate.

Unlike casting or other conventional manufacturing methods, materials produced by additive manufacturing can experience different thermal histories between layers. The variation in thermal history can in turn lead to different local microstructures, consequently affecting the precipitation process. Highly distorted areas favor Chromium segregation and therefore ease the structure transformation from austenite to sigma phase. The mechanism of the σ-phase formation depends on microstructure, chemical composition, temperature and time duration of the ageing treatment. In fact, the small size of the dendrites gives raise to a high grain boundaries surface, which considerably speed up the diffusion process even at room temperature [25, 39].

As already stated, this alloy is a solid Nitrogen supersaturated solution and, as a consequence of repeated thermal cycles, nitrides are nucleated, which however have extremely small dimensions due to the fast cooling rate, figure 9 and 11. These small precipitates are difficult to detect or to chemically characterize e.g. to distinguish between $Cr_2N$ and CrN in EDS analyses.

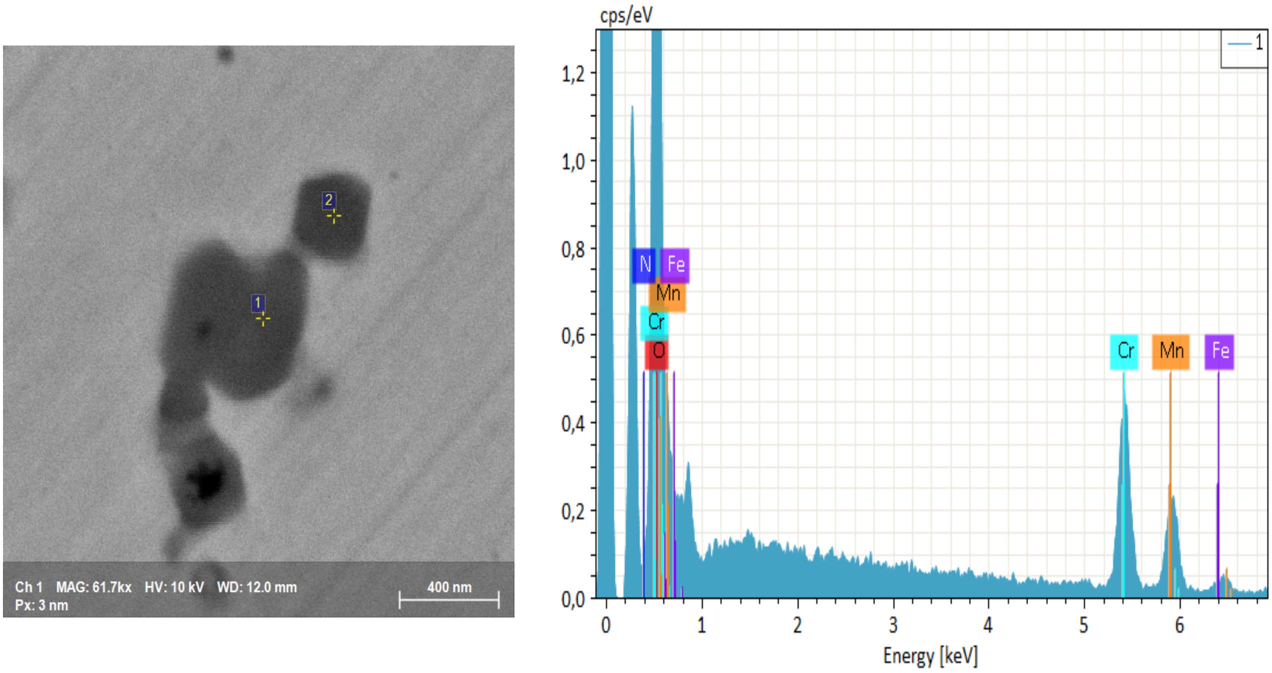

(**a**) (**b**)

**Figure 11.** (a) SEM FEG high resolution precipitates image. (b) EBDS spectrum of the rounded sigma phase.

### *3.3. Microstructure evolutions of selective laser-melted equiatomic CoCrFeMnNi high-entropy alloy after cold rolling and aging in the 723 K-1423 K temperature range.*

As reported in several recent studies, a second phase can appear in this alloy after annealing [13, 27, 39]. Owing due to that, the microstructural evolution of this alloy when subjected to prolonged annealing times is studied. To better evaluate the microstructural evolution and the second phases precipitation, we followed two different paths. The first is annealing on as built samples, the second is annealing after cold rolling deformation, which speeds up precipitation phenomena at the edge of new and smaller equiaxed grains by recrystallization. The alloy behavior results to be the same as regard precipitates formation and composition, except that recrystallization occurs at a lower temperature in cold rolled samples. An interesting question, at this point, is: will the second phase precipitation be favored in SLM over the alloy produced by casting? Will it be compositionally and structurally different or similar? Depending on that, the two alloys would exhibit different behaviors in high temperature exercise. Figures 12, 13 and 14 show the alloy microstructure of cold deformed samples, annealed at 1173 K for 100 h samples, cold deformed and heated at 1173 K for 100 h samples, respectively.

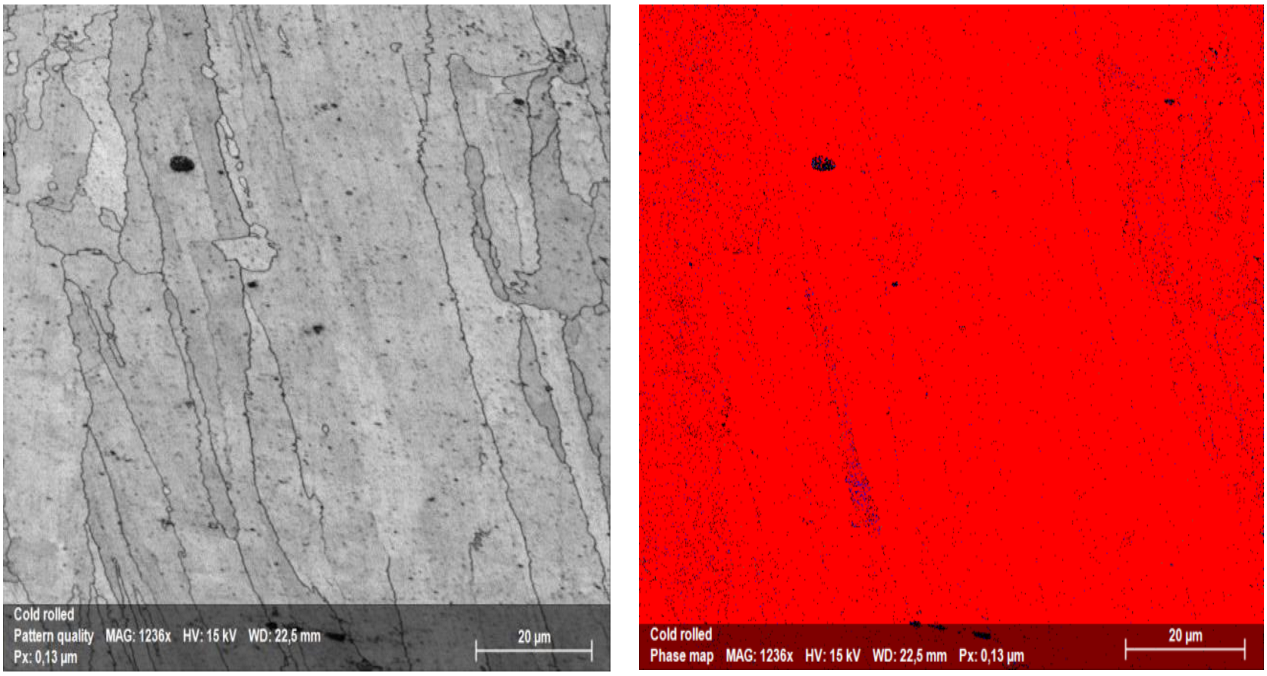

(**a**) (**b**)

**Figure 12.** (a) Cross-sectional image of a cold rolled sample. (b) corresponding EBDS map, with FCC matrix in red and sigma phase precipitates in blue.

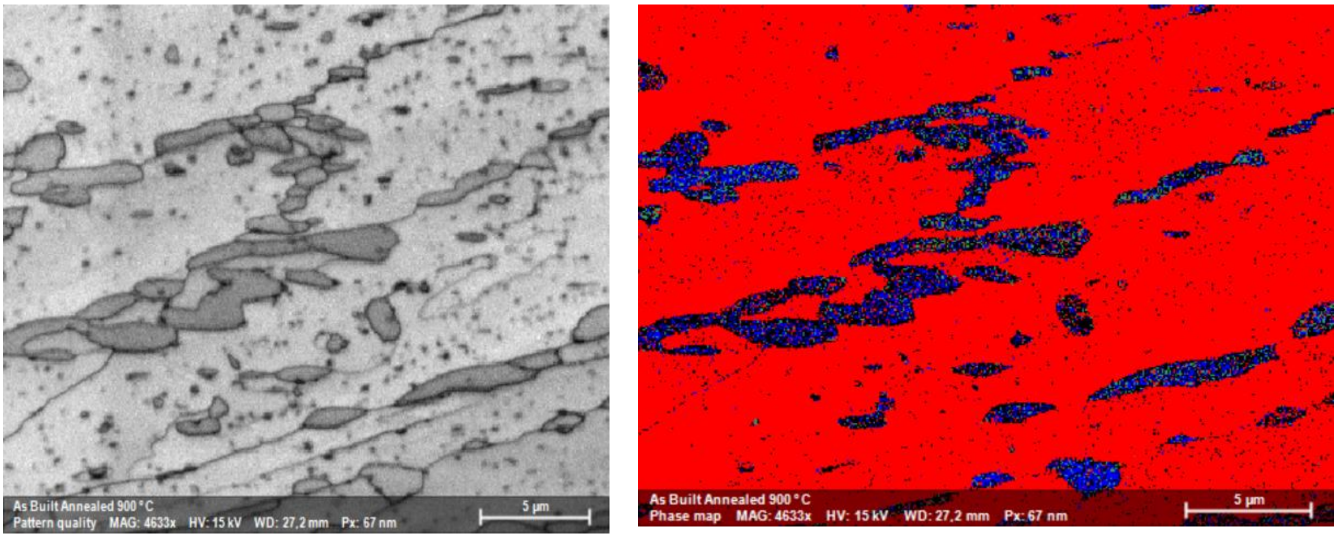

(**a**) (**b**)

**Figure 13.** (a) Cross-sectional image of an as built sample annealed at 1173 K for 100 h. (b) corresponding EBDS map, with FCC matrix in red and sigma phase precipitates in blue.

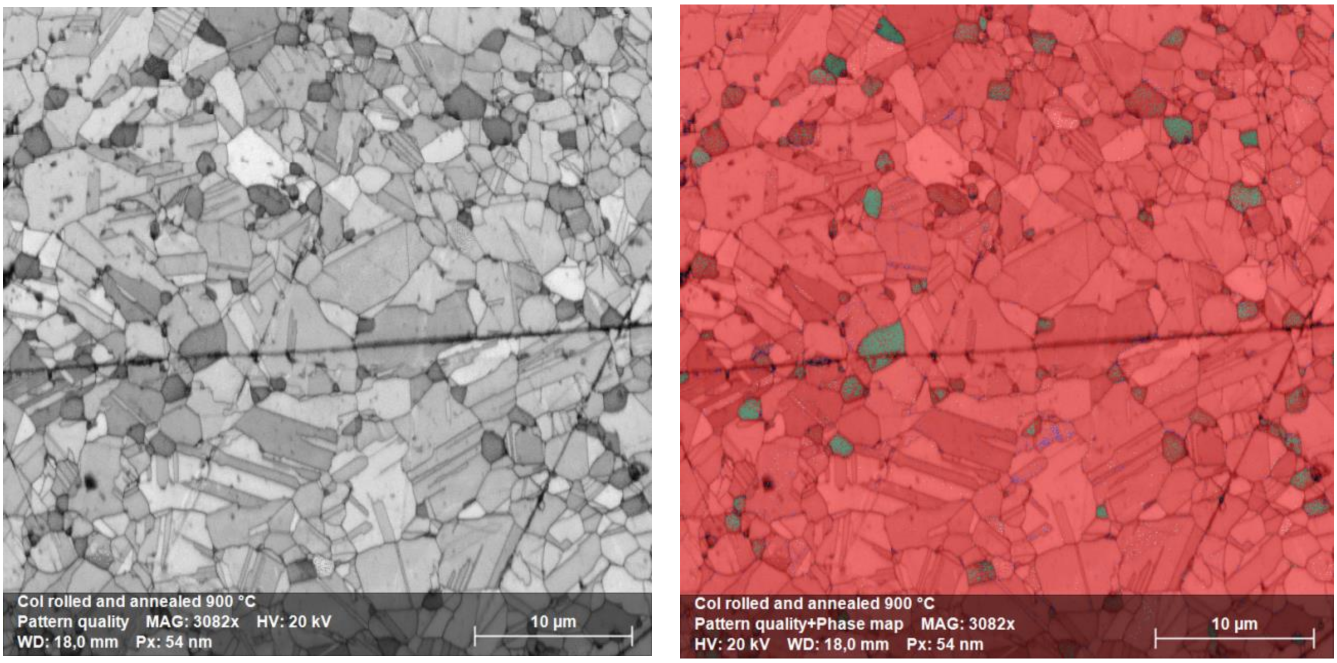

(**a**) (**b**)

**Figure 14.** (a) Cross-sectional image of a cold rolled and annealed for 100 h at 1173 K sample. (b) corresponding EBDS map, with FCC matrix in red and precipitates in green.

The cross-sectional image of figure 12a shows the typical elongated grain microstructure of a cold rolled sample. There is no evidence of cracks or voids. The corresponding EBSD map of figure 12b reveals an FCC matrix (red) and a very thin tetragonal sigma phase (blue), not detected in XRD, figure 2. The sample annealed for 100 h at 1173 K, figure 13a, retains the same elongated microstructure except for the sigma phase, whose grains increase in size. This is particularly evident in the EBSD map of figure 13b where the same colors as before are used. Up to the recrystallization temperature there is no particular difference in the microstructural morphology and secondary precipitation phases between cold rolled and annealed samples.

The precipitation effect becomes more evident when recrystallization occurs, as shown in figure 14. The original columnar grains become rounded and, due to increased diffusion rates, the sigma phase grains grow in size while remaining preferentially located at the FCC grain boundaries. The diffraction spectrum continues to show the majority sigma phase alone, figure 15.

The semi-quantitative chemical analysis of the recrystallized FCC phase reveals how it is depleted of Cr and Mn leaving unchanged, with respect to the as produced alloy, the atomic composition of the other elements. On the contrary, the precipitation phase is enriched with Cr and N while depleted in Fe, Co Ni and Mn, as can be seen from the EDS composition in tables 2 and 3. This is observed for both the samples of figure 13 and figure 14 [40,41]. XRD measures confirm the presence in the samples of an FCC matrix and of a Cr-rich phase, figure 8.

Let consider now in greater details what happens on cold rolled samples as a function of the annealing temperature. The microstructural evolution due to annealing at 723 K, 823 K, 923 K, 1023 K, 1123 K, 1223 K, 1323 K and 1423 K for 25 h, result to be a quite complex process. Figure 6 and figure 7 show optical and scanning electron microscopy transversal section images of this process, respectively. Up to 923 K, the optical and scanning electron microscopy analysis reveal that the microstructure always consists of an FCC solid solution with a chemical composition close to the starting equiatomic one, as reported in the semiquantitative EDS analyses of table 2. The metallographic observations in optical and electron microscopy made on samples aged at 723 K, 823 K and 923 K, figure 6, confirm the presence of a fine precipitation at the grain boundaries. As far as the SLM

HEA has a predominant microstructure made of ultra-fine grains with abundant grain boundaries, a Cr-N rich sigma phase precipitation is expected. The small size of these precipitates however does not provide a sufficient scattering volume to allow to detect this phase by XRD diffraction.

Things start to change when the recrystallization process occurs, that is above 1023 K. Precipitates (sigma phase) are now clearly observed. They are found to consist of a Cr – (Co,Mn,Fe,Ni N)-rich phase together with a significant increase in Nitrogen, see table 3. The structure is that of a body centered tetragonal lattice, which embrittles the alloy.

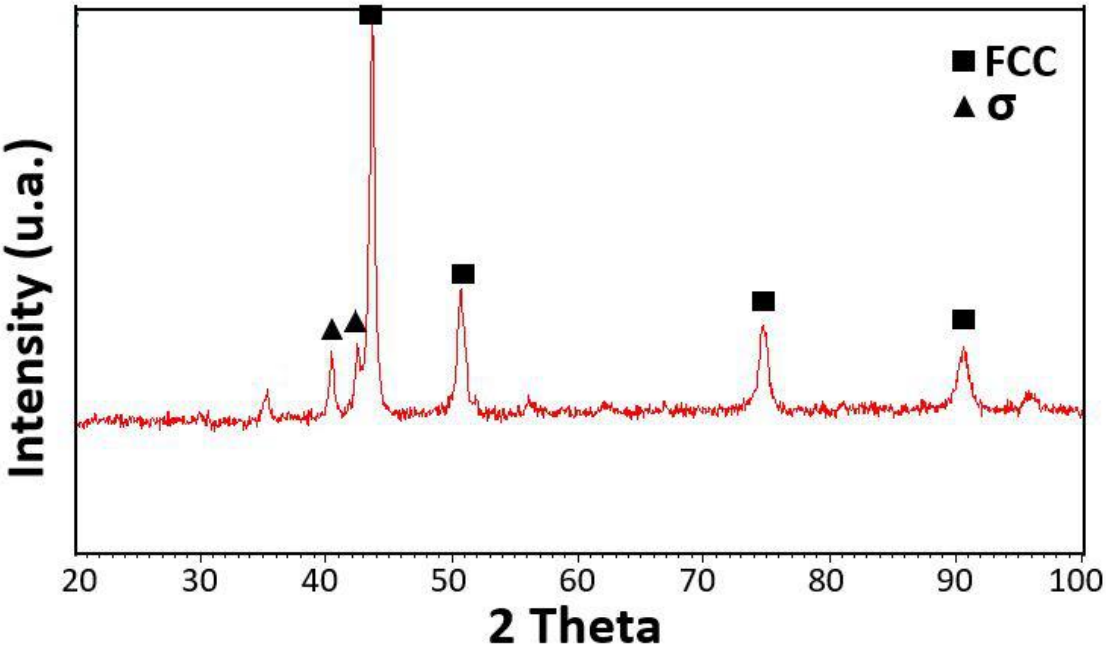

**Figure 15.** diffraction pattern on a sample annealed at 1173 K for 100h

**Table 2.** EDS semi-quantitative chemical compositions, in atomic %, of FCC matrix of cold rolled samples.

| Temperature (K) | Nitrogen | Chromium | Manganese | Iron | Cobalt | Nickel |
|---|---|---|---|---|---|---|
| As cast | 1.2 | 19.8 | 14.4 | 21.7 | 22 | 20.9 |
| 723 | 0 | 19.7 | 16.3 | 22.5 | 21.7 | 19.8 |
| 823 | 1 | 18.9 | 17.5 | 20.5 | 21 | 21 |
| 923 | 0.6 | 18.2 | 15.3 | 22 | 22.4 | 21.5 |
| 1023 | 3 | 15.6 | 16.6 | 21.8 | 22 | 21 |
| 1123 | 1.1 | 14.2 | 16 | 23 | 23.4 | 22.3 |
| 1223 | 1.7 | 10.9 | 16.4 | 23.7 | 24.3 | 23 |
| 1323 | 1.3 | 10.8 | 17 | 24.1 | 24.1 | 22.7 |
| 1423 | 1.7 | 18.2 | 14 | 21.3 | 22.6 | 22.2 |

Preprints (www.preprints.org) | NOT PEER-REVIEWED | Posted: 21 June 2022 doi:10.20944/preprints202206.0295.v1

**Table 3.** EDS semi-quantitative chemical compositions, in atomic %, of sigma phase of cold rolled samples.

| Temperature (K) | Nitrogen | Chromium | Manganese | Iron | Cobalt | Nickel |
|---|---|---|---|---|---|---|
| 923 | 1.4 | 19 | 16 | 21 | 21.8 | 20.8 |
| 1023 | 2.9 | 27.1 | 14.7 | 19 | 18.6 | 17.7 |
| 1123 | 9 | 39.3 | 10.7 | 14.9 | 13.7 | 12.4 |
| 1223 | 17 | 56.9 | 8.2 | 7 | 5.9 | 5 |
| 1323 | 22.5 | 45.1 | 8.7 | 9 | 7.8 | 6.9 |
| 1423 | 6.1 | 24 | 13 | 19 | 19.5 | 18.4 |

Generally, this phase is believed to have an $A_xB_y$ formula, with x and y approximately equal [42, 43]. Cr has been identified as the major forming element, and it is found with a concentration of ~ 50 at.%. Hence, σ particles can be described as an ideal solid solution in which Cr atoms are the solutes while the other elements constitute the matrix. However, from the EDS results alone, it is not possible to determine unambiguously whether other phases, such as μ, χ, Cr-rich ferrite (α′), carbides or Laves phases, sometimes observed in standard FCC HEAs, are present [44].

A significant precipitation is observed in the samples heat treated at 1023 K or above. It is a coarse sigma phase located at triple points of the recrystallized alloy. If the recrystallization is carried out at 1323 K for 25 h, then there is also precipitation inside the FCC grains, close to the geminates, suggesting that these locations are preferential nucleation sites when the aging temperature increases, as reported in figure 6 and figure 7. The electron backscatter diffraction microstructures of figure 14b shows, as a significant example, the phase map of the recrystallized alloy at 1173 K which identifies a predominantly FCC alloy, red color, with geminates and a secondary sigma phase precipitation.

From a general point of view, precipitate sizes are found to increase with either increasing aging time and temperature. Therefore, it seems reasonable that the activation energy value of the σ-phase precipitation be the sum of three different contributions, i.e. those of lattice, pipe, and interphase boundary diffusion having high, intermediate, and low activation energies, respectively. The precipitation is the result of two phenomena (nucleation and growth) which are affected by the alloy microstructure. Therefore, further experimental work focusing on nucleation and coarsening is required to fully understand this process.

The X-ray diffraction patterns of the cold-rolled and annealed samples below the recrystallization temperature (up to 923 K) remain the same, as shown in figure 8. Diffraction peaks from the matrix due to a single FCC phase are observed in all the samples up to 1423 K, but when the annealing temperature reaches 1023 K, low-intensity diffraction peaks belonging to the σ phase can also be detected. The appearance of low-intensity diffraction peaks due to the σ phase is also reported by other authors [45].

The heterogeneous nature of nucleation significantly increases the rate of nucleation for temperatures close to equilibrium. Consequently, the growth of nuclei implies two distinct phenomena: (1) atoms jump of both phases from one side of the interface to the other and (2) atoms diffusion from the solid solution towards the precipitate. Depending on which process is prevalent, the precipitation process will be controlled by interface phenomena or by diffusion. As suggested by our observations of a temperature dependent precipitation kinetics, which is consistent with a diffusion mechanism, it seems that the precipitation growth be the result of the shift from one mechanism to the other, with diffusion becoming the prevalent one. In fact, EDS analyses of high temperature annealed samples reveal a significant Cr depletion of the FCC structure, together with a Cr enrichment in the precipitates. Cr depletion in the FCC phase also correlates with a significant increase in the alloy grain size with the aging temperature, see figure 5 and table 2.

Precipitates observed after annealing at a temperature of 1323 K bear some resemblance to dendritic growth: they consist of plates or needles which lie on certain crystallographic planes of the matrix and which preferentially grow in length by slightly modifying their transverse dimensions, as shown in figure 6 and figure 7. This kind of precipitate, that occurs inside the enlarged grains, is consistent with the idea that diffusion at the grain boundaries and volume diffusion have similar speed. When the grains are larger, Cr atoms must diffuse over longer distances in order to reach the grain boundary.

This shape evolution in precipitates anticipates their dissolution occurring at 1423 K, as shown in the micrographs of figure 6 and figure 7 and in the corresponding XRD spectra, where the new coarse grains are almost completely devoid of precipitates. After annealing at 1423 K, the semi-quantitative composition provided by EDS confirms that the alloy becomes substantially monophasic with FCC lattice and a chemical composition which is approximately that of the starting equiatomic alloy, with the usual exception of Mn.

In the electron backscattering image of figure 7, the correlation between grain size and precipitate size is clearly visible: the smaller the grain, the larger the number of precipitates because grain boundary diffusion is favored. On the contrary, when aging temperature is higher than 1323 K, it is found a significant presence of precipitates between the FCC coarse grains. It is reasonable to think that volume diffusion at temperatures $T \geq 1323$ K preferentially occurs along high-density lattice planes because these are the most widely spaced planes.

In summary, fine precipitates are present in as-built samples. Their size gradually increases with annealing temperature up to 1323 K to subsequently decrease at higher annealing temperatures. Annealing temperature also affects composition and the place of formation of the precipitates: at the triple points of the grain boundaries when the alloy recrystallizes (1023 K or above); along the columnar grain boundaries with rounded shape below 1023 K. Moreover, the annealing time required to accomplish precipitation is greater than 25 h.

### 3.4. Mechanical behavior: microhardness measures.

Figure 16 shows the microhardness of HEAs SLM samples before and after prolonged annealing treatments in the 723-1423 K temperature range. The microhardness increases significantly with cold rolling and after annealing, mostly at 723 K or 823 K. This is reasonably due to the previously mentioned fine precipitation at the grain boundaries. At higher temperatures, annealing leads to a significant change in the volume fraction of the $\sigma$ phase, whose maximum is observed around 1200 K.

At 923 K a softening effect begins, also documented by the Cr depletion in the FCC solid solution, as shown in table 2, which causes a reduction in microhardness value in comparison with that of specimens annealed at lower temperatures. It should be reminded that deformation twinning is reported in the literature for CoCrFeMnNi as a mechanism of room temperature deformation [46, 47].

When annealing at 1023 K the alloy recrystallizes and this brings about a microhardness increase. Subsequent annealing at higher temperatures entails an increase of both precipitates and FCC grains. This in turn leads to a progressive microhardness reduction up to the complete dissolution of the sigma phase into a single FCC solid solution. The result follows the classical Hall–Petch relationship.

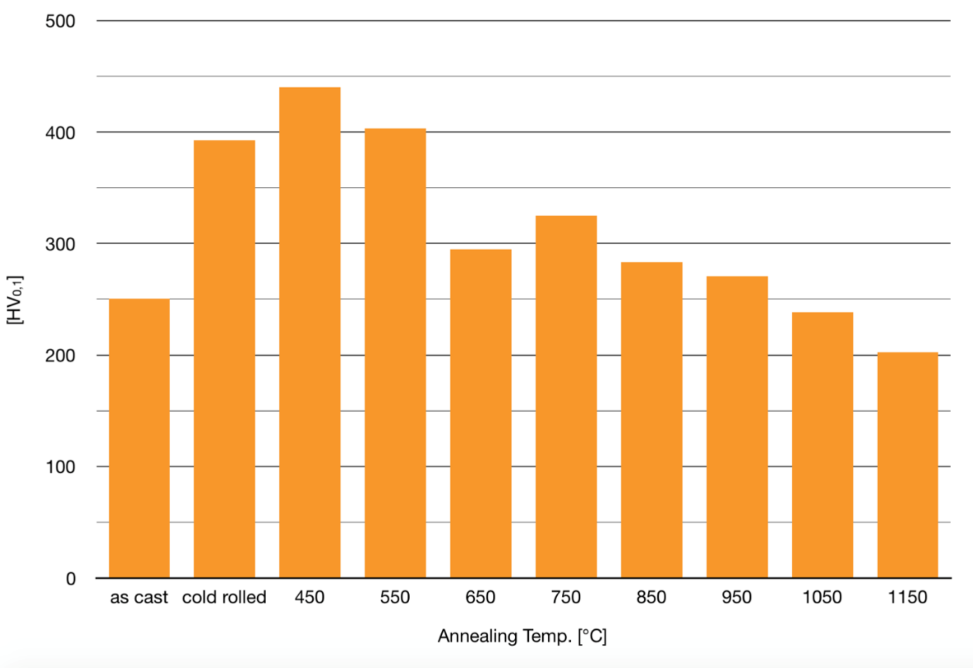

**Figure 16.** Microhardness of cold rolled and annealed samples at temperature from 723 K to 1423 K.

Correlating with the microstructural and XRD investigations, these mechanical tests can provide important information on the stability and metastability of these high entropy alloys.

## 4. Conclusions

Unlike what has been observed for the classical Cantor alloys obtained by casting technology [48], where precipitation of secondary phases occurs after thousands of hours annealing at high temperatures, the alloy obtained by SLM does not require prolonged exposure to high temperature to produce the same phenomenon. Instead SLM technology induces a fine secondary phases precipitation of nitrides and intermetallic phases in as built state.

The most significant phenomenon observed in this study is the complex decomposition tendency of the Cantor's alloy in annealing conditions. The cold rolled plus annealed FCC matrix, within the limits of temperatures and time examined, becomes unstable and secondary phases precipitate. The observed precipitation is made of tetragonal Cr-rich sigma phase and of mixed Cr (Fe,Mn,Co,Ni)-nitrides which nucleate at the triple points. The size of the sigma phase precipitates increases with annealing temperature because it is a diffusion-controlled process. When the annealing temperature is below the recrystallization temperature, the size of precipitates is small due to a low diffusion rate and confined at the boundaries of the as built dendritic structure. In the annealing thermal range 1023 K-1323 K, apart from recrystallization of the FCC phase, precipitates formation is observed at the grain boundary. When the temperature exceeds 1323 K the σ phase dissolves (unlike precipitations attributable to nitrides) and the alloy substantially returns single phase with near equiatomic composition.

σ phase and nitride precipitations yield a significant alloy hardening only for annealing up to 923 K, that is below recrystallization temperature. Recrystallization, favored by cold rolling, induces, in the 1023 K-1323 K thermal range, the precipitation of a Chromium and Nitrogen rich phase. This effect leads to a progressive hardness reduction of the alloy as a function of annealing temperature which can be understood recalling that Cr is a strong hardener in solid solutions, together with grain swelling.

These experimental results suggest that thermodynamic databases and models need to be extended and improved to better understand this complex kind of alloy. Further studies are also needed to determine the Time-Temperature-Precipitation curve in order to become able to predict the precipitation kinetics, like in the case of austenitic stainless steels. A careful investigation of the precipitation processes is particularly important in view of the use of HEAs for structural applications, because intermetallic precipitation phases and nitrides are generally known to be embrittling phases. This observed phase instability of the CoCrFeMnNi HEA suggests that care needs to be given to the alloy exercise temperature.

**Author Contributions:** Conceptualization, E.G.C and. A.C.; formal analysis, E.G.C and. A.C.; investigation, A.C.; resources, A.C.; writing—original draft preparation, A.C; writing—review and editing, E.G.C.; All authors have read and agreed to the published version of the manuscript."

**Funding:** This research received no external funding

**Conflicts of Interest:** The authors declare no conflict of interest

## References

1. Cantor B. Multicomponent high-entropy Cantor alloys. *Progress in Materials Science* **2021** 120, 100754. https://doi.org/10.1016/j.pmatsci.2020.100754.
2. Cantor B.; Chang I.; Knight P.; Vincent A. Microstructural development in equiatomic multicomponent alloys. *Mater. Sci. Eng. A* **2004** 375-377, 213-218. doi: 10.1016/j.msea.2003.10.257.
3. Yeh, J.W.; Chen, S.K.; Lin, S.J.; Gan, J.Y.; Chin, T.S.; Shun, T.T.; Tsau, C.H.; Chang, S.Y. Nanostructured high-entropy alloys with multiple principal elements: Novel alloy design concepts and outcomes. *Adv. Eng. Mater.* **2004**, *6*, 299–303, doi:10.1002/adem.200300567.
4. Miracle, D.B.; Senkov, O.N.; Wilks, J. A critical review of high entropy alloys and related concepts. *Acta Mater.* **2017**, *122*, 448–511. https://doi.org/10.1016/j.actamat.2016.08.081
5. Kao, Y.F.; Chen, T.J.; Chen, S.K.; Yeh, J.W. Microstructure and mechanical property of as-cast, homogenized and deformed $Al_xCoCrFeNi$ ($0 \leq x \leq 2$) high-entropy alloys. *J. Alloys Compd.* **2009**, *488*, 57–64. Doi: 10.1016/j.jallcom.2009.08.090.
6. Poletti, M.G.; Fiore, G.; Battezzati, L. Development of a new high entropy alloy for wear resistance: $FeCoCrNiW_{0.3}$ and $FeCoCrNiW_{0.3}$ + 5 at. % of C. *Mater. Des.* **2017**, *115*, 247–254, doi: 10.1016/j.matdes.2016.11.027.
7. Miracle, D.; Senkov, O.N.; Wilks, G.B.; Scott, J.M. Mechanical properties of Nb25Mo25Ta25W25 and V20Nb20Mo20Ta20W20 refractory high entropy alloys. *Intermetallics* **2011**, *19*, 698–706, doi: 10.1016/j.intermet.2011.01.004.
8. Tabachnikova, E.D.; Podolskiy, A.V.; Laktionova, M.O.; Bereznaia, N.A.; Tikhonovsky, M.A.; Tortika, A.S. Mechanical properties of the $CoCrFeNiMnV_x$ high entropy alloys in temperature range 4.2–300 K. *J. Alloys Compd.* **2017**, *698*, 501–509, doi: 10.1016/j.jallcom.2016.12.154.
9. B. Gludovatz B., A. Hohenwarter A., D. Catoor D., Chang E.H., George E.P., Ritchie R.O. *A fracture-resistant high-entropy alloy for cryogenic applications*. Science, **2014** 345, 1153-1158. DOI: 10.1126/science.1254581
10. Kao, Y.F.; Lee, T.D.; Lee, P.H.; Chang, Y.S. Electrochemical passive properties of $Al_xCoCrFeNi$ (x = 0, 0.25, 0.50, 1.00) alloys in sulfuric acids. *Corros. Sci.* **2010**, *52*, 1026–1034, doi: 10.1016/j.corsci.2009.11.028.
11. Yeh, J.W. Alloy design strategies and future trends in high-entropy alloys. *JOM* **2013**, *65*, 1759–1771. https://doi.org/10.1007/s11837-013-0761-6
12. Zhang, Y.; Zuo, T.T.; Tang, Z.; Gao, M.C.; Dahmen, K.A.; Liaw, P.K.; Lu, Z.P. Microstructures and properties of high-entropy alloys. *Prog. Mater. Sci.* **2014**, *61*, 1–93, doi.org/10.1016/j.pmatsci.2013.10.001.
13. Bhattacharjee, P.P.; Sathiaraj, G.D.; Zaid, M.; Gatti, J.R.; Lee, C.; Tsai, C.W.; Yeh, J.W. Microstructure and texture evolution during annealing of equiatomic CoCrFeMnNi high-entropy alloy *J. Alloys Compd.*, **2014**, 587, 544-552
14. Otto, F.; Dlouhy, A.; Somsen, C.; Bei, H.; Eggeler, G.; George, E.P. The influences of temperature and microstructure on the tensile properties of a CoCrFeMnNi high-entropy alloy. *Acta Mater.* **2013**, *61*, 5743–5755.
15. Otto, F.; Hanold, N.L.; George, E.P. Microstructural evolution after thermomechanical processing in an equiatomic, single-phase CoCrFeMnNi high-entropy alloy with special focus on twin boundaries *Intermetallics*, **2014** 54, 39-48. https://doi.org/10.1016/j.intermet.2014.05.014.
16. Sathiaraj G.D.; Bhattacharjee P.P.; Tsai C.W.; Yeh, J.W. Effect of heavy cryo-rolling on the evolution of microstructure and texture during annealing of equiatomic CoCrFeMnNi high entropy alloy. *Intermetallics*, **2016** 69, 1-9.
17. Liu, W. H.; Lu, Z. P.; He, J. Y.; Luan, J. H.; Wang, Z. J.; Liu, B.; Yong Liu; Chen, M. W.; Lui, C. T. Ductile $CoCrFeNiMo_x$ high entropy alloys strengthened by hard intermetallic phases. *Acta Materialia* **2016** 116, 332-342. https://doi.org/10.1016/j.actamat.2016.06.063.
18. He, J.Y.; Wang, H.; Huang, H.L.; Xu, X.D; Chen, M.W.; Wu, Y.; Liu, X.J.; Nieh, T.G.; An, K.; Lu, Z.P. A precipitation-hardened high-entropy alloy with outstanding tensile properties. *Acta Mater.* **2016** 102, 187-196. DOI: 10.1016/j.actamat.2015.08.076.

19. Olakanmi, E.O.; Cochrane, R.F.; Dalgarno, K.W. A review on selective laser sintering/melting (SLS/SLM) of aluminium alloy powders: processing, microstructure, and properties *Prog. Mater. Sci.* **2015** 74, 401-477. ISSN 0079-6425.
20. Rao, H.; Giet, S.; Yang, K.; Wu, X.; Davies, C.H.J. The influence of processing parameters on aluminium alloy A357 manufactured by Selective Laser Melting *Mater. Des*., **2016** 109, 334-346. Doi: 10.1016/j.matdes.2016.07.009.
21. Moravcik, I.; Kubicek, A.; Moravcikova-Gouvea, L.; Ondrej, A.; Kana, V.; Pouchly, V.; Zadera, A.; Dlouhy, I. The Origins of High-Entropy Alloy Contamination Induced by Mechanical Alloying and Sintering. *Metals* **2020**, *10*, 1186. https://doi.org/10.3390/met10091186
22. DebRoy, T.; Wei, H.L.; Zuback, J.S.; Mukherjee, T.; Elmer, J.W.; Milewski, J.O.; Beese, A.M.; Wilson-Heid, A.; De, A.; Zhang, W. Additive manufacturing of metallic components-process, structure and properties. *Prog. Mater. Sci.* **2018** 92, 112-224
23. Li, X.P.; Wang, X.J.; Saunders, M.; Suvorova, A.; Zhang, L.C.; Liu, Y.J.; Fang, M.H.; Huang, Z.H.; Sercombe, T.B. A selective laser melting and solution heat treatment refined Al-12Si alloy with a controllable ultrafine eutectic microstructure and 25% tensile ductility. *Acta Mater*., **2015** 95, 74-82. Doi: 10.1016/j.actamat.2015.05.017.
24. Brif, Y.; Thomas, M.; Todd, I. The use of high-entropy alloys in additive manufacturing. *Scripta Mater*. **2015** 99, 93-96. https://doi.org/10.1016/j.scriptamat.2014.11.037.
25. Li, R.; Niu, P.; Yuan, T.; Cao, P.; Chen, C.; Zhou, K. Selective laser melting of an equiatomic CoCrFeMnNi high-entropy alloy: processability, non-equilibrium microstructure and mechanical property. *J. Alloy. Comp*. **2018** 746, 125-134. DOI: 10.1016/j.jallcom.2018.02.298.
26. Tsai, K.Y.; Tsai, M.H.; Yeh J.W. Sluggish diffusion in Co-Cr-Fe-Mn-Ni high-entropy alloys. *Acta Mater*. **2013** 61,4 887-4897. http://dx.doi.org/10.1016/j.actamat.2013.04.058.
27. Schuh, B.; Mendez-Martin, F.; Völker, B.; George, E.P.; Clemens, H.; Pippan, R.; Hohenwarter, A. Mechanical properties, microstructure and thermal stability of a nanocrystalline CoCrFeMnNi high-entropy alloy after severe plastic deformation. *Acta Mater.* **2015** 96, 258-268. https://doi.org/10.1016/j.actamat.2015.06.025.
28. Guo, J.; Minhao, G.; Zhiguang, Z.; Xiaohua, L.; Mui Ling Sharon, N.; Jun Wei On the machining of selective laser melting CoCrFeMnNi high-entropy alloy. *Mater. Des.* **2018,** 153**,** 211–220. https://doi.org/10.1016/j.matdes.2018.05.012.
29. Chew, Y. *et al*. Microstructure and enhanced strength of laser aided additive manufactured CoCrFeMnNi high entropy alloy. *Mater. Sci. Eng. A* **2019** 744, 137–144. https://doi.org/10.1016/j.msea.2018.12.005.
30. Xiang, S. *et al*. Effects of process parameters on microstructures and tensile properties of laser melting deposited CrMnFeCoNi high entropy alloys. *Mater. Sci. Eng. A* **743**, 412–417 (2019). https://doi.org/10.1016/j.msea.2018.11.110.
31. Xiang, S. *et al*. Microstructures and mechanical properties of CrMnFeCoNi high entropy alloys fabricated by using laser metal deposition technique. *J. Alloy. Compd.* **2019** 773, 387–392. https://doi.org/10.1016/j.jallcom.2018.09.235.
32. Zhu, Z. G. *et al*. Hierarchical microstructure and strengthening mechanism of a CoCrFeMnNi high entropy alloy additively manufactured by selective laser melting. *Scr. Mater.* **2018** 154, 20–24. https://doi.org/10.1016/j.scriptamat.2018.05.015.
33. Colombini, E.; Lassinantti Gualtieri, M.; Rosa, R.; Tarterini, F.; Zadra, M.; Casagrande, A.; Veronesi, P. SPS-assisted Synthesis of SICp reinforced high entropy alloys: reactivity of SIC and effects of pre-mechanical alloying and post-annealing treatment, *Powder Metallurgy*, **2017** 61, 64-72. DOI: 10.1080/00325899.2017.1393162
34. Luke, N.; Carter, C. M.; Whiters, P.J.; Attallah, M.M. The influence of the laser scan strategy on grain structure and cracking behaviour in SLM powder-bed fabricated nickel superalloy. *J. Alloys Compd*., **2014**, 615, 338-347. https://doi.org/10.1016/j.jallcom.2014.06.172.
35. Kim, Y. K.; Choe, J.; Lee, K. A.; Selective laser melted equiatomic CoCrFeMnNi high-entropy alloy: microstructure, anisotropic mechanical response and multiple strengthening mechanism *J. Alloys Compd*. **2019** 805, 680–91. DOI: 10.1016/j.jallcom.2019.07.106.
36. Otto, F.; Yang, Y.; Bey, H.; George, E. Relative effects of enthalpy and entropy on the phase stability of equiatomic high-entropy alloys. *Acta Mater*. **2013** 61, 2628-2638. https://doi.org/10.1016/j.actamat.2013.01.042.
37. Nilsson, J. O.; Chai, G. The physical metallurgy of duplex stainless steels. In *Proceedings of the Duplex Stainless Steel Conference*, Beaune, France, 13–15 October **2010**.
38. Dubiel, B.; Sieniawski, J. Precipitates in Additively Manufactured Inconel 625 Superalloy. *Materials* **2019** 12, 1144. https://doi.org/10.3390/ma12071144.
39. Otto, F.; Dlouhý, A.; Pradeep, K.G.; Kubenova, M.; Raabe, D.; Eggeler, G.; George, E.P. Decomposition of the single-phase high-entropy alloy CrMnFeCoNi after prolonged anneals at intermediate temperatures. *Acta Mater.* **2016** 112, 40-52. Doi: /10.1016/j.actamat.2016.04.005.
40. Wang, W.F.; Wu, M.J. Effect of silicon content and aging time on density, hardness, toughness and corrosion resistance of sintered 303LSC–Si stainless steels. *Mater. Sci. Eng. A* **2006** 425, 167-171. https://doi.org/10.1016/j.msea.2006.03.050.
41. Zhao, W. X.; Zhou, D. Q.; Jiang, S. H.; Wang, H.; Wu, Y.; Liu, X. J.; Wang, X. Z.; Lu, Z. P. Ultrahigh stability and strong precipitation strengthening of nanosized NbC in alumina-forming austenitic stainless steels subjecting to long-term high-temperature exposure. *Mat. Sci. and Engineering. A* **2018** https://doi.org/10.1016/j.msea.2018.09.081.
42. Hall, E.O.; H. Algie, S.H. The Sigma Phase. *Metallurgical reviews*. **1966** 11, 61-88. https://doi.org/10.1179/mtlr.1966.11.1.61
43. Sully, A.H. The sigma phase in binary alloys of the transition elements. *Journal of the Institute of Metals*. **1951** 80, 173.
44. Laplanche, G.; Berglund, S.; Reinhart, C.; Kostka, A.; Fox, F.; George, E.P. *Acta Materialia* 2018 161, 338-351. https://doi.org/10.1016/j.actamat.2018.09.040.
45. Warren, A.D.; Harniman, R.L.; Guo, Z.; Younes, C.M.; Flewitt, E.J.; Scott, T.B. Quantification of sigma-phase evolution in thermally aged 2205 duplex stainless steel. *Journal of Materials Science* **2016** 51, 694–707. DOI: 10.1007/s10853-015-9131-9.

46. Moravcik, I.; Hornik, V.; Minárik, P.; Li, L.; Dlouhy, I.; Janovska, M.; Raabe, D.; Li, Z. Interstitial doping enhances the strength-ductility synergy in a CoCrNi medium entropy alloy, *Mater. Sci. Eng. A* **2020** 781, 139242. https://doi.org/10.1016/j.msea.2020.139242.
47. George, E.P.; Curtin, W.A.; Tasan, C.C. High entropy alloys: A focused review of mechanical properties and deformation mechanisms, *Acta Mater*. **2020** 188, 435–474. https://doi.org/10.1016/j.actamat.2019.12.015
48. Campari, E.G.; Casagrande, A.; Colombini, E.; Lassinanti Gualtieri, E.; Veronesi, P. The Effect of Zr Addition on Melting Temperature, Microstructure, Recrystallization and Mechanical Properties of a Cantor High Entropy Alloy. *Materials* **2021** 14, 5994. https://doi.org/10.3390/ma14205994.